Computer Physics Communications 266 (2021) 108027

Contents lists available at ScienceDirect

Computer Physics Communications

www.elsevier.com/locate/cpc

# AICON2: A program for calculating transport properties quickly and accurately ☆,☆☆

Tao Fan *, Artem R. Oganov

*Skolkovo Institute of Science and Technology, Bolshoy Boulevard 30, bld. 1, 121205 Moscow, Russia*

ARTICLE INFO

*Article history:*
Received 4 September 2020
Received in revised form 21 March 2021
Accepted 18 April 2021
Available online 12 May 2021

*Keywords:*
Electrical conductivity
Seebeck coefficient
Relaxation time approximation
Electron-phonon coupling

ABSTRACT

Calculating the transport properties, such as electrical conductivity, has been a great challenge in materials modeling fields because of its complexity. We have implemented an algorithm to calculate the electronic transport properties using the generalized Kane band model and perturbation theory in the framework of the relaxation time approximation. Three scattering mechanisms affect the total relaxation time: acoustic phonon scattering, polar optical phonon scattering, and ionized impurity scattering. All the necessary parameters can be calculated from first principles. The capability of the program was tested on a group of semiconductors, and the obtained results show reasonable agreement with experiment. The program works fast, and is robust and especially appropriate for high-throughput screening of thermoelectric materials.

**Program summary**
*Program title:* AICON2
*CPC Library link to program files:* https://doi.org/10.17632/s9b8y8t92c.2
*Code Ocean capsule:* https://codeocean.com/capsule/7509547
*Licensing provisions:* GPLv3
*Programming language:* Python3
*External routines/libraries:* Numpy, Scipy, spglib, pymatgen, atomate, emc
*Nature of problem:* Calculation of electrical and thermal conductivity from first principles requires a large number of computing resources in order to construct electron-phonon coupling matrix elements, integrate over the Brillouin zone and construct high-order force constants matrix.
*Solution method:* Combining the perturbation theory with the deformation potential theory to calculate the electronic transport properties, using the modified Debye-Callaway model to calculate the phonon transport properties.



## 1. Introduction

The first version of AICON (Ab Initio Conductivities) provided a robust and highly efficient method (modified Debye-Callaway model) for calculating the lattice thermal conductivity [1], which is helpful in such fields as thermoelectricity, thermal barrier coatings and heat sinks, and in planetary sciences. The new version of the program, AICON2, adds functions for calculating electronic transport properties, such as electrical conductivity, Seebeck coefficient etc., which enables AICON2 to do both electron and phonon transport calculations. The program is fast and relatively accurate.

Electronic transport properties, such as electrical conductivity, are fundamental in various scientific and technological applications. For example, a thermoelectric material should be a good conductor to achieve a high figure of merit, whereas other applications like piezoelectric materials require an insulator. Theoretically, electrical conductivity can be calculated on the basis of modern density functional

☆ The review of this paper was arranged by Prof. J. Ballantyne.
☆☆ This paper and its associated computer program are available via the Computer Physics Communications homepage on ScienceDirect (http://www.sciencedirect.com/science/journal/00104655).
* Corresponding author.
*E-mail address:* Tao.Fan@skoltech.ru (T. Fan).

https://doi.org/10.1016/j.cpc.2021.108027
0010-4655/

theory (DFT) and density functional perturbation theory (DFPT). Several programs, such as BoltzTraP [2], BoltzWann [3], and PERTURBO [4], have already been released for this purposes. Among them, BoltzTraP and BoltzWann are based on the semiclassical transport theory with the constant relaxation time approximation (CRTA). They differ in the method of interpolating the bands: the former uses the Fourier expansion of the band energies with symmetry being kept by star functions, the latter utilizes the maximally localized Wannier functions (MLWF) basis to interpolate plane wave results. Although these calculations are easier and faster than a fully ab initio method, CRTA itself is a rough approximation, because the relaxation time, which is usually a function of temperature and chemical potential, cannot be considered constant. PERTURBO employs an iterative solution of the linearized Boltzmann transport equation (BTE) and does not require any empirical parameters to calculate the conductivity. However, in order to make the calculations converge, the electron-phonon matrix elements need to be computed on extremely dense $\boldsymbol{k}$- and $\boldsymbol{q}$-point meshes in the Brillouin zone, which makes the calculations too expensive. Besides the mentioned methods of calculating the transport properties, there is another, much easier way based on the deformation potential theory.

In 1950, Bardeen and Shockley have proposed the deformation potential theory to calculate mobilities in non-polar crystals [5], which is based on assumptions that energy surface is isotropic, electrons only interact with the acoustic phonon modes with long wavelengths, and the local deformations produced by the lattice waves are similar to those in homogeneously deformed crystals. Therefore, a matrix element of the interaction between electrons and phonons can be formulated with a key parameter, the deformation potential constant $E_1$. This constant can be calculated from the variation in the energy band edges with lattice constant. Later, Herring and Vogt have generalized this theory to include anisotropy in the scattering processes for semiconductors with multiple nondegenerate band edges [6]. The energy surface for each band edge point is assumed to be ellipsoidal, whereas the strength of the electron-phonon interaction is still characterized by the deformation potential constant. However, there are two deformation potential constants, $E_d$ and $E_u$, in this generalized method, and they can be obtained from fitting experimental data. The authors applied this method to calculate charge carrier mobilities in n-type germanium and silicon, and the results were in reasonable agreement with the observations. Based on the generalized Kane band model and perturbation theory, Ravich et al. have developed a method to calculate the transport properties and analyze the experimental data in lead chalcogenides [7,8]. In this method, four scattering mechanisms, including acoustic phonon scattering, polar optical phonon scattering, impurity scattering, and collisions between carriers, are mainly considered, and all necessary parameters can be obtained from experiment. The calculated transport coefficients showed quite close agreement with the experimental values in a wide range of temperatures and carrier concentrations. A lot of applications have been developed in recent years on the basis of Ravich's method [9–13], verifying its reliability.

With the release of AICON2, we aim to achieve three goals. First, we want to expand the capabilities of the software. It implements an algorithm to calculate the electronic transport properties of semiconductors based on Ravich's method, and all the key parameters can be calculated utilizing modern first-principles methods without using any empirical values. With this expansion, our software can do both electron and phonon transport calculations for bulk materials. Second, to make the program more easily expanded and called, and to bring it more in line with the object-oriented programming guidelines, the implementation of functions is based on class instead of function. Finally, in order to reduce the workload of researchers in the calculating process, an automated workflow management has been achieved with the help of open source workflow software [14,15]. Such an implementation is especially friendly to high-throughput calculations.

The paper is structured as follows. In Section 2 we introduce the theory and the mathematical formalism for electronic transport properties. Section 3 includes three examples as an illustration of the capability of our code. We present our main conclusions and discuss future directions for development in Section 4.

## 2. Methodology

### 2.1. Semiclassical transport theory

AICON2 can compute electronic transport properties in the framework of the semiclassical BTE. Assuming the material is homogeneous and the relaxation time $\tau$ is independent of the direction of the crystal momentum $\boldsymbol{k}$ when the external field is weak, according to the relaxation time approximation (RTA), all the transport coefficients can be expressed in terms of some averaged quantities, namely $\langle \tau^l z^q \rangle$ [7]:

$$\left\langle \tau^l z^q \right\rangle = \frac{\int_0^\infty (-\frac{\partial f}{\partial z})[\frac{\tau(z)}{m_d^*(z)}]^l z^q k^3 \, \mathrm{d}z}{\int_0^\infty (-\frac{\partial f}{\partial z}) \frac{k^3}{m_{d_0}^{*l}} \, \mathrm{d}z} \tag{1}$$

where $f = 1/(\mathrm{e}^{(\varepsilon-\eta)/k_B T}+1)$ is the Fermi-Dirac distribution function; $z = \varepsilon/k_B T$ is the reduced band energy, $k_B$ is the Boltzmann constant, $T$ is the temperature; $m_{d_0}^*$ is the density of states (DOS) effective mass at the band edge, while $m_d^*$ is the DOS effective mass at energy $z$; $l$ and $q$ are constants. The parameters $\tau$, $k$, and $m_d^*$ are all functions of $z$, and their detailed expressions are given later.

Therefore, the formulas for carrier mobility $\mu$, carrier concentration $n$, electrical conductivity $\sigma$, Seebeck coefficient $\alpha$, Hall factor $A$, Hall coefficient $R$, Lorenz number $L_0$, and electronic thermal conductivity $\kappa_e$ are:

$$\mu = \frac{e\,\langle \tau \rangle}{m_c^*} \tag{2}$$

$$n = \frac{(2m_{d_0}^* k_B T)^{3/2}}{3\pi^2 \hbar^3} \int_0^\infty (-\frac{\partial f}{\partial z})(z+\beta z^2)^{3/2} \, \mathrm{d}z \tag{3}$$

$$\sigma = ne\mu \tag{4}$$

$$\alpha = \frac{k_B}{e} \frac{\langle \tau(z-\zeta) \rangle}{\langle \tau \rangle} \tag{5}$$

$$A = \frac{3K(K+2)}{(2K+1)^2}\frac{\langle\tau^2\rangle}{\langle\tau\rangle^2} \tag{6}$$

$$R = \frac{A}{en} \tag{7}$$

$$L_0 = \left(\frac{k_B}{e}\right)^2 \left\{\frac{\langle\tau z^2\rangle}{\langle\tau\rangle} - \left[\frac{\langle\tau z\rangle}{\langle\tau\rangle}\right]^2\right\} \tag{8}$$

$$\kappa_e = L_0 T\sigma \tag{9}$$

where $e$ is the elementary charge and $\hbar$ is the Planck constant; $\zeta = \eta/k_BT$ is the reduced chemical potential; $m_c^*$ is the conductivity effective mass; $K$ is the ratio of the effective mass $m_\parallel^*/m_\perp^*$, reflecting the anisotropy of the band.

### 2.2. Modified Kane band model

In the Kane band model, the constant energy surface for any energy value is assumed to be ellipsoidal. It is also assumed that the longitudinal and transverse effective masses of electrons and holes are governed by the interaction of the lowest conduction band with the highest valence band, whereas the contributions of other bands are negligibly small. This model is also called a "two-band" model. The relationship between the energy and crystal momentum is expressed as [7,8]

$$\frac{\hbar^2k_\perp^2}{m_{\perp0}^*} + \frac{\hbar^2k_\parallel^2}{2m_{\parallel0}^*} = \varepsilon\left(1+\frac{\varepsilon}{\varepsilon_g}\right) \tag{10}$$

here $\varepsilon_g$ is the band gap; $k_\perp$ and $k_\parallel$ are the transverse and longitudinal components of the momentum $\boldsymbol{k}$; $m_{\perp0}^*$ and $m_{\parallel0}^*$ are the transverse and longitudinal components of the effective mass tensor at the band edge. The part in parentheses indicates the nonparabolicity of the band. Then, the energy dependence of the effective mass is

$$m_i^* = m_{i0}^*\left(1+\frac{2\varepsilon}{\varepsilon_g}\right) = m_{i0}^*(1+2\beta z) \tag{11}$$

where $\beta = k_BT/\varepsilon_g$, $i$ denotes $\parallel$ or $\perp$. The DOS effective mass is expressed as

$$m_d^* = N^{2/3}m_b^* = N^{2/3}(m_\parallel^* m_\perp^{*2})^{1/3} \tag{12}$$

here $N$ is the degeneracy of the band due to the symmetry. The conductivity effective mass is

$$\frac{1}{m_c^*} = \frac{1}{3}\left(\frac{1}{m_\parallel^*} + \frac{2}{m_\perp^*}\right) \tag{13}$$

When the effective mass is known, the value of the momentum $k$ can be defined as

$$k(z) = \frac{(2k_BTm_{b_0}^*)^{1/2}}{\hbar}[z(1+\beta z)]^{1/2} \tag{14}$$

and the density of states is

$$\rho(z) = \frac{(2k_BT)^{1/2}m_{d_0}^{*3/2}}{\pi^2\hbar^3}[z(1+\beta z)]^{1/2}(1+2\beta z) \tag{15}$$

Although the model is called "two-band" model, sometimes bands besides valence band maximum (VBM) and conduction band minimum (CBM) should also be considered. For example, for p-type PbTe, there is a second band near the VBM in energy and this band becomes dominant at high temperatures. In our model, one more band can be taken into account for n- or p-type semiconductors if it exists. Such a band is assumed to be independent of CBM or VBM.

### 2.3. Scattering mechanisms for relaxation time of electrons

Three scattering mechanisms — acoustic phonon scattering, polar optical phonon scattering, and ionized impurities scattering — are considered here, with corresponding relaxation times $\tau_{aco}$, $\tau_{opt}$, and $\tau_{imp}$. The total relaxation time is found by summing these relaxation times according to Matthiessen's rule:

$$\frac{1}{\tau} = \frac{1}{\tau_{aco}} + \frac{1}{\tau_{opt}} + \frac{1}{\tau_{imp}} \tag{16}$$

Here we only present the final expressions for each relaxation time and discuss the parameters involved and application range of each mechanism. Detailed derivations can be found in the literature [7,8].

*2.3.1. Acoustic phonon scattering*

At high temperatures and carrier densities, scattering by acoustic phonons predominates. The strength of the acoustic phonon scattering can be represented by the deformation potential constants, and the corresponding relaxation time is almost isotropic. The main expression for this type of scattering was originally provided by Bardeen [5] and is widely used. Ravich added the effect of band nonparabolicity as well as the dependence of the matrix element of the interaction of carriers with the acoustic phonons on the energy in the nonparabolic region. The formula is given by [8]

$$\frac{1}{\tau_{aco}(z)} = \frac{\pi k_B T \rho \Xi^2}{\hbar c N}\left[1 - \frac{8\beta(z+\beta z^2)}{3(1+2\beta z)^2}\right] \tag{17}$$

where $\Xi$ is the deformation potential constant; $c$ is the elastic constant related with longitudinal and transverse acoustic wave velocity. The factor in brackets describes the energy dependence of the squared matrix element of the electron-phonon interaction.

*2.3.2. Polar optical phonon scattering*

In a polar crystal, at some temperatures the polar scattering by the long-wavelength longitudinal optical phonons gives rise to approximately the same temperature dependence as the acoustic phonon scattering. The polar scattering is strongly inelastic at low temperatures. However, it can be regarded as almost elastic above the compound's Debye temperature, and the relaxation time concept can be used. As in the case of the acoustic phonon scattering, nonparabolicity should be allowed. Moreover, since the density of free carriers in real applications is always high, it screens the electric field produced by optical vibrations in polar crystals. This screening effect reduces the strength of the polar scattering and should also be included. The formula for the polar scattering is [8]

$$\begin{aligned}\frac{1}{\tau_{opt}(z)} = {} & \frac{2^{1/2} k_B T e^2 m_{b_0}^{*1/2}(\varepsilon_\infty^{-1} - \varepsilon_0^{-1})}{\hbar^2 (z k_B T)^{1/2}} \frac{1+2\beta z}{(1+\beta z)^{1/2}} \\ & \times \left\{\left[1 - \delta \ln\left(1+\frac{1}{\delta}\right)\right] - \frac{2\beta(z+\beta z^2)}{(1+2\beta z)^2}\left[1 - 2\delta + 2\delta^2 \ln\left(1+\frac{1}{\delta}\right)\right]\right\}\end{aligned} \tag{18}$$

where $\varepsilon_\infty$ and $\varepsilon_0$ are the high-frequency and static dielectric constants; $\delta = (2kr_\infty)^{-2}$ with the screening radius $r_\infty$ of the medium with $\varepsilon_\infty$:

$$r_\infty^{-2} = \frac{4\pi e^2 \rho(z)}{\varepsilon_\infty} \tag{19}$$

*2.3.3. Ionized impurities scattering*

Scattering by ionized impurities and vacancies is the dominant mechanism at very low (liquid helium) temperatures in highly degenerate samples. It is described by the formula [7]

$$\frac{1}{\tau_{imp}(\zeta)} = \frac{2e^4 N m_{b_0}^*(1+2\beta\zeta)\Phi(\delta_0)}{3\pi\varepsilon_0^2\hbar^3} \tag{20}$$

where $\Phi(\delta_0)$ is the logarithmic factor:

$$\Phi(\delta_0) = \ln(1+\delta_0^{-1}) - (1+\delta_0)^{-1} \tag{21}$$

with $\delta_0 = (2k_F r_0)^{-2}$ and $r_0$ is the screening radius of a medium with dielectric constant $\varepsilon_0$. In highly degenerate samples

$$r_0^{-2} = \frac{4\pi e^2 \rho(\zeta)}{\varepsilon_0} \tag{22}$$

where $\rho(\zeta)$ is the density of states at the reduced chemical potential $\zeta$ and $k_F$ is expressed in terms of the carrier concentration for one valley:

$$k_F = \left(\frac{3\pi^2 n}{N}\right)^{1/3} \tag{23}$$

The concentration of carriers is in the simplest case equal to the concentration of impurities. Relaxation time $\tau_{imp}$ is a function of chemical potential, which is different from $\tau_{aco}$ and $\tau_{opt}$. In the implementation of this code, to get the total relaxation time, $\tau_{aco}$ and $\tau_{opt}$ are first added and applied in Eq. (1) to transform to a function of chemical potential, the result is then added to $\tau_{imp}$.

*2.3.4. Deformation potential constant*

The deformation potential constant is a key parameter for the relaxation time of the acoustic phonon scattering. It can be calculated as [5]

$$\Xi_i = \frac{\Delta E_{i,V}}{\Delta l_V} \tag{24}$$

where $\Delta E_{i,V}$ is the energy difference of band edge $i$ at volume $V$; $\Delta l_V$ is the volumetric strain and it is dimensionless. When such a strain is small, it can be assumed that the same band edge belonging to different volumes has the same reference energy; thus, these energies can be compared directly. Three calculations of the band energies of a given material should be done: one at the equilibrium volume, the other two at slightly larger volumes. Then, our code can calculate the deformation potential constants of each band edge automatically.

*2.3.5. Elastic constant*

The elastic constant $c$ is also an important parameter for the relaxation time of the acoustic phonon scattering. Whereas only longitudinal acoustic wave was considered in Bardeen's work, here we take into account contributions from both longitudinal and transverse acoustic waves. Using the Voigt-Reuss-Hill approximation [16–18], the bulk modulus $B$ and shear modulus $G$ can be calculated:

$$B_{\mathrm{V}} = \frac{(C_{11}+C_{22}+C_{33})+2(C_{12}+C_{23}+C_{31})}{9} \tag{25a}$$

$$G_{\mathrm{V}} = \frac{(C_{11}+C_{22}+C_{33})-(C_{12}+C_{23}+C_{31})+3(C_{44}+C_{55}+C_{66})}{15} \tag{25b}$$

$$\frac{1}{B_{\mathrm{R}}} = (S_{11}+S_{22}+S_{33})+2(S_{12}+S_{23}+S_{31}) \tag{25c}$$

$$\frac{1}{G_{\mathrm{R}}} = \frac{4(S_{11}+S_{22}+S_{33})-4(S_{12}+S_{23}+S_{31})+3(S_{44}+S_{55}+S_{66})}{15} \tag{25d}$$

$$B_{\mathrm{H}} = \frac{B_{\mathrm{V}}+B_{\mathrm{R}}}{2} \tag{25e}$$

$$G_{\mathrm{H}} = \frac{G_{\mathrm{V}}+G_{\mathrm{R}}}{2} \tag{25f}$$

where $C$ and $S$ are the elastic constant matrix and its inverse matrix. Then the acoustic phonon velocity can be obtained:

$$v_L = \left(\frac{B_{\mathrm{H}}+4/3G_{\mathrm{H}}}{\rho}\right)^{1/2} \tag{26a}$$

$$v_T = \left(\frac{G_{\mathrm{H}}}{\rho}\right)^{1/2} \tag{26b}$$

$$\frac{1}{v_m} = \frac{1}{3}\left(\frac{1}{v_L}+\frac{2}{v_T}\right) \tag{26c}$$

where $\rho$ is the mass density of the compound and $v_m$ is the average phonon velocity. The direction-averaged elastic constant $c$ is calculated as

$$c = \rho v_m^2 \tag{27}$$

*2.3.6. Effective mass of the band edge*

The effective mass at the band edge can be calculated using the finite difference method as implemented in Effective Mass Calculator (EMC) [19]. In our program, a modification of the original EMC code was made to obtain the effective masses internally during the calculation of the transport coefficients.

*2.4. Workflow and technical issues*

*2.4.1. Workflow*

The input parameters required by the "two-band" model include the deformation potential constants, effective mass tensor, dielectric constants, and elastic constants, which can all be calculated by DFT. The workflow of calculating the electronic transport coefficients is shown in Fig. 1. After finishing the DFT calculations, AICON2 collects the information from the corresponding directories and obtains the necessary input parameters automatically. Then the transport coefficients are calculated and output in a specific format.

*2.4.2. Technical issues*

AICON2 is implemented in Python 3, and is incompatible with Python 2. The code can be called either from a command-line interface or from a script. For calculating the electronic transport properties, the program can be run in two modes: 'standard' or 'doping'. The 'standard' mode calculates and outputs the transport coefficients as a function of specified temperature at default chemical potential values. The chemical potential starts from the middle of the gap and goes to the level that is 1 eV higher with a step of 2 meV. The 'doping' mode calculates and outputs the results as a function of specified temperature and carrier concentration. To calculate the lattice thermal conductivity, only the temperature needs to be specified.

The program stores results as pandas.DataFrame object, which is very flexible and easy to manipulate, analyze, and plot the data. It can also be saved in any file format supported by pandas [20].

The workflow of electronic transport property calculation is shown in Fig. 1. Before running AICON2, the user needs to carry out DFT calculations with VASP code. Band structure calculation at three different volumes (one at equilibrium volume, the other two at a bit larger volumes) is for determining deformation potential constants. Effective mass calculation is for determining effective masses at CBM and VBM (also second band if exists). Dielectric constant calculation is for determining high-frequency and static dielectric constants. Elastic constant calculation is for determining elastic constant tensor. After these calculations finished, the resulting files (such as vasprun.xml) should be collected into a directory and the naming rule should be exactly the same as the examples distributed with our code. Then, AICON2 can be called either from command-line or python script to calculate the transport properties. As indicated in the figure, at least 13 DFT calculations need to be done. Although each of them is relatively simple, managing the workflow becomes an intensive task, which involves checking the results of each step and copying the necessary files from the last step. To alleviate this problem for high-throughput calculation, in AICON2 we also implemented an automatic workflow tools based on pymatgen [21], Atomate [14]and FireWorks [15].

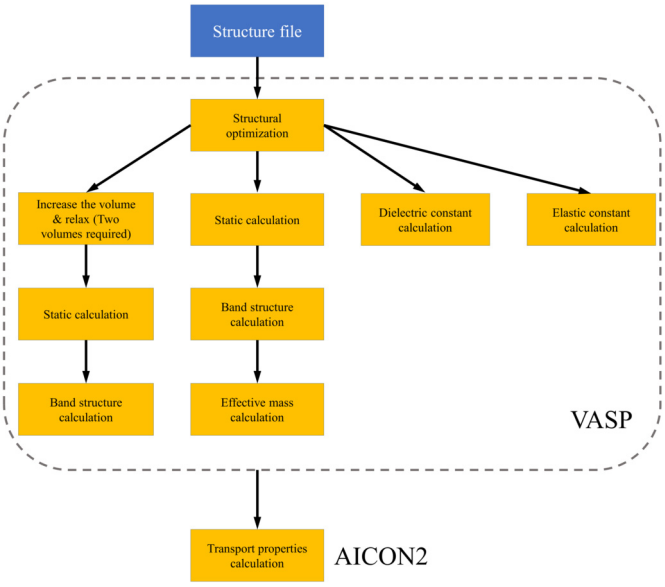


**Fig. 1.** Workflow of the electronic transport properties calculation using AICON2.

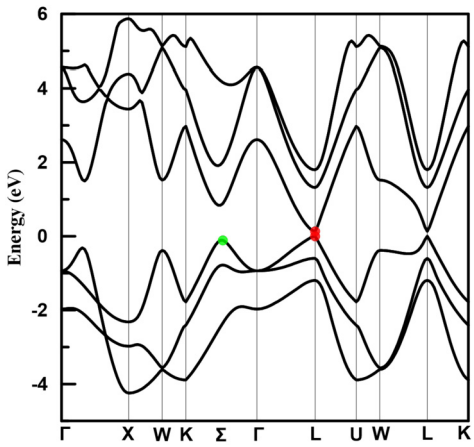


**Fig. 2.** Band structure of PbTe. The CBM and VBM are shown by red points. The second highest valence band edge is indicated by a green point. (For interpretation of the colors in the figure(s), the reader is referred to the web version of this article.)

The users only need to provide structural files and some necessary settings for each DFT calculation, then the whole workflow can run automatically. Besides, it is convenient to build users' own databases this way.

The API of AICON2 is referenced in its source code and in the documented examples provided with the source distribution.

### 2.5. Updated model for lattice thermal conductivity

We have updated the model for lattice thermal conductivity. In our last paper, lattice thermal conductivity $\kappa$ was calculated as [1]:

$$\kappa = \frac{c_V^{aco}}{c_V^{aco}+c_V^{opt}} \times (\kappa_{LA}+\kappa_{TA}+\kappa_{TA'}) + \frac{c_V^{opt}}{c_V^{aco}+c_V^{opt}} \times \kappa_O \tag{28a}$$

$$\kappa_i = \kappa_{i1} + \kappa_{i2} \quad (i = TA, TA', LA, O) \tag{28b}$$

$$\kappa_{i1} = \frac{1}{3} C_i T^3 \int_0^{\theta_i/T} \frac{\tau_C^i(x) x^4 e^x}{(e^x-1)^2}\, dx \tag{28c}$$

$$\kappa_{i2} = \frac{1}{3} C_i T^3 \frac{\left[\int_0^{\theta_i/T} \frac{\tau_C^i(x) x^4 e^x}{\tau_N^i(x)(e^x-1)^2}\, dx\right]^2}{\int_0^{\theta_i/T} \frac{\tau_C^i(x) x^4 e^x}{\tau_N^i(x)\tau_R^i(x)(e^x-1)^2}\, dx} \tag{28d}$$

**Table 1**
Key parameters of PbTe, calculated and experimental [8,10], at the conduction band minimum (CBM), valence band maximum (VBM), and second valence band (VSB). $m_{\parallel}^*$ and $m_{\perp}^*$ the longitudinal and the transverse component of the effective mass tensor, $m_c^*$ the conductivity effective mass, $m_d^*$ the DOS effective mass, $\Xi$ the deformation potential constant, $N$ the band degeneracy, $E_g$ the band gap, $c$ the direction-averaged elastic constant, $\varepsilon_\infty$ and $\varepsilon_0$ the high-frequency and static dielectric constants.

| | | $m_{\parallel}^*$ ($m_e$) | $m_{\perp}^*$ ($m_e$) | $m_c^*$ ($m_e$) | $m_d^*$ ($m_e$) | $\Xi$ (eV) | $N$ | $E_g$ (eV) | $c$ (GPa) | $\varepsilon_\infty$ | $\varepsilon_0$ |
|---|---|---|---|---|---|---|---|---|---|---|---|
| CBM | Calc. | 0.069 | 0.025 | 0.032 | 0.089 | 10.28 | 4 | 0.13 | 32.43 | 26 | 446 |
| | Exp. | 0.240 | 0.024 | 0.034 | 0.130 | 19 | 4 | 0.3 | 31.2 | 33 | 400 |
| VBM | Calc. | 0.076 | 0.029 | 0.037 | 0.101 | 12.10 | 4 | 0.13 | 32.43 | 26 | 446 |
| | Exp. | 0.310 | 0.022 | 0.032 | 0.134 | 19 | 4 | 0.3 | 31.2 | 33 | 400 |
| VSB | Calc. | 2.341 | 0.123 | 0.150 | 1.721 | 11.33 | 12 | 0.24 | 32.43 | 26 | 446 |
| | Exp. | 0.382 | 0.382 | 0.382 | 2 | 9.5 | 12 | 0.36 | 31.2 | 33 | 400 |

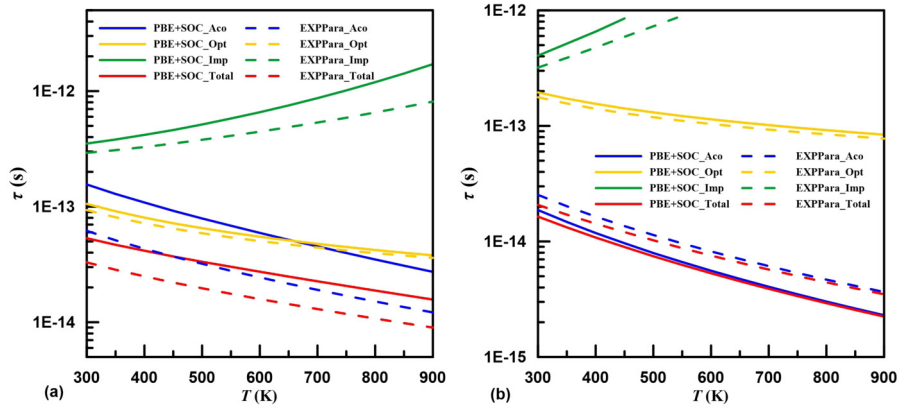


**Fig. 3.** Relaxation time for (a) n-type and (b) p-type PbTe calculated at $n = 1.8 \times 10^{19}$ cm$^{-3}$ and $p = 2.5 \times 10^{20}$ cm$^{-3}$, respectively. The two kinds of results (PBE+SOC and EXPPara) correspond to two kinds of key parameters listed in Table 1.

where $c_V^{aco}$ and $c_V^{opt}$ are specific heat of acoustic and optical branches, $\theta_i$ is the Debye temperature for each phonon branch, $C_i = k_B^4/(2\pi^2\hbar^3 v_i)$ and $x = \hbar\omega/k_B T$. $\tau_N^i$ is the relaxation time of the normal phonon process, $\tau_R^i$ is the total relaxation time of all the resistive scattering processes, and $(\tau_C^i)^{-1} = (\tau_N^i)^{-1} + (\tau_R^i)^{-1}$. Detailed description of these parameters can be found in our previous paper.

According to our recent tests, this model overestimates the contribution from optical branches. Especially, for those compounds with low lattice thermal conductivity, the calculated $\kappa$ is usually overestimated. Therefore, we now adopt a new formula:

$$\kappa = \kappa_{LA} + \kappa_{TA} + \kappa_{TA'} + \kappa_O \tag{29}$$

The formulae for $\kappa_{TA}$, $\kappa_{TA'}$ and $\kappa_{LA}$ are the same as before, while that for $\kappa_O$ becomes

$$\kappa_O = \frac{1}{3}(3p-3)\frac{N}{V}k_B f_E\left(\frac{\Theta_E}{T}\right)v_O^2\tau_C^O\left[1+\frac{\tau_R^O}{\tau_N^O}\right] \tag{30a}$$

$$f_E(x) = x^2\frac{e^x}{(e-1)^2} \tag{30b}$$

where $p$ is the number of atoms in primitive cell; thus, $3p-3$ is the number of optical phonon branches. $N$ is the number of primitive cells (usually, $N = 1$), $V$ is the volume of the primitive cell, $v_O$ is the average velocity of optical phonon, and $\Theta_E$ is the Einstein temperature. The function $f_E$ is the so called Einstein function. The formula for calculating $\tau_N^O$, $\tau_R^O$, and $\tau_C^O$ are assumed the same as those of longitudinal acoustic branch.

The new model preforms well for a wide range of materials. See the supplementary materials for tests.

## 3. Examples

Here three representative materials — PbTe, SnSe (both low and high temperature phases) and $Bi_2Te_3$ — are shown in order to demonstrate the capabilities of AICON2. In supplementary material, we also list data for other test materials. All first-principles calculations were performed using the VASP code with the projector-augmented wave (PAW) method [22,23]. The exchange-correlation energy was approximated by the PBE-GGA functional [24]. For structure relaxation, the plane wave kinetic energy cutoff was set to 600 eV and the Brillouin zone was sampled using Γ-centered meshes with the reciprocal-space resolution of 0.03 Å$^{-1}$. Kohn-Sham equations were solved self-consistently with total energy tolerance of $10^{-7}$ eV/cell and structures were relaxed until the maximum force became smaller than $10^{-3}$ eV/Å. The dielectric constants were calculated using the DFPT method [25], the elastic constants were calculated using the finite difference method as implemented in VASP. To get the deformation potential constants, three band structure calculations were run: one at the equilibrium volume, the other two at volumes larger by 0.1% and 0.2%. For PbTe and $Bi_2Te_3$, spin-orbit coupling (SOC) effect was

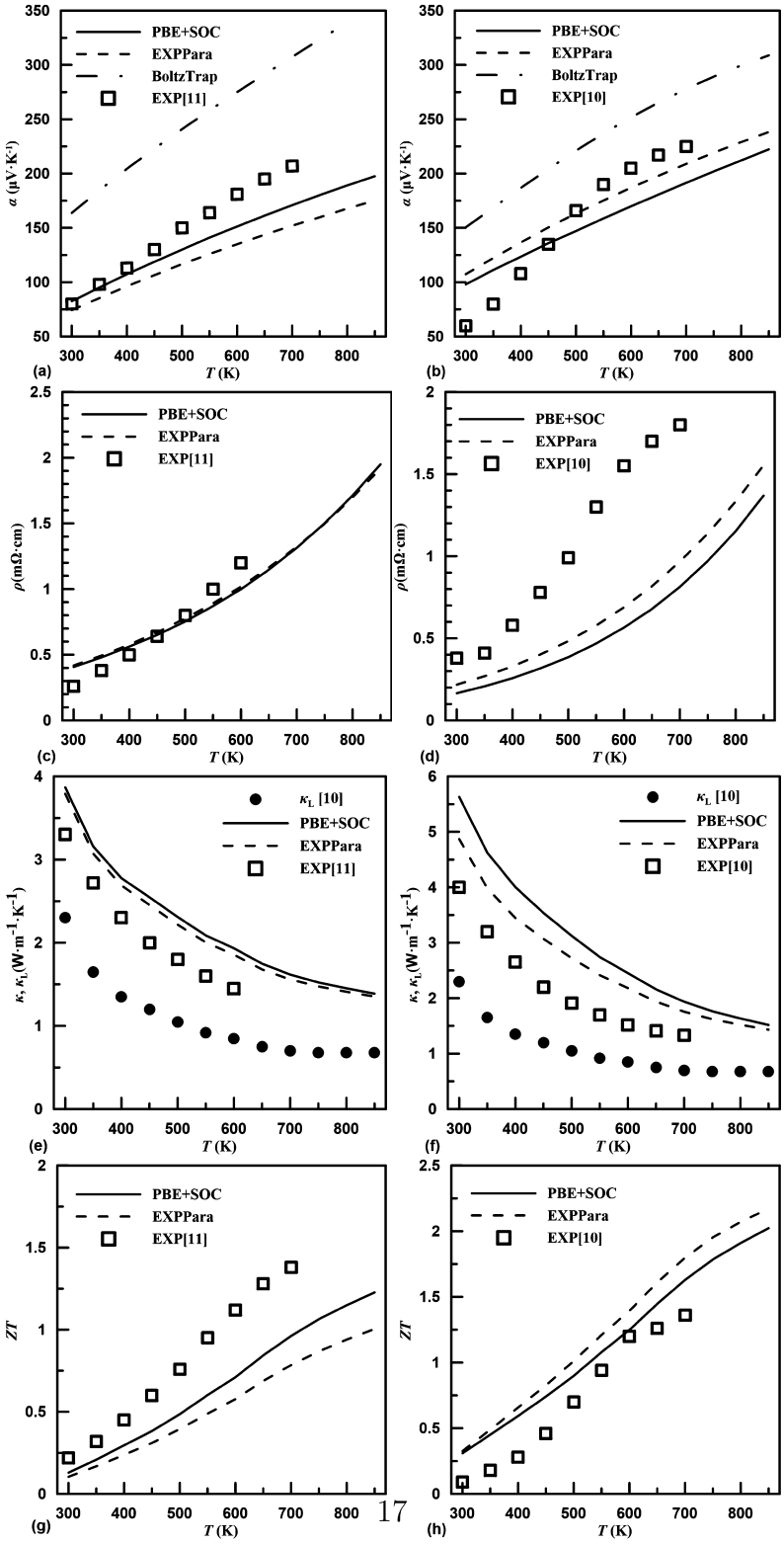


**Fig. 4.** Transport properties for n-type (left) and p-type (right) PbTe calculated at $n = 1.8 \times 10^{19}$ cm$^{-3}$ and $p = 2.5 \times 10^{20}$ cm$^{-3}$, respectively.

included in all band related calculations. For SnSe and $Bi_2Te_3$, the van der Waals correction [26] was included because these materials have layered structures. The detailed settings can be found in the example directory within the distribution package.

### 3.1. Lead telluride (PbTe)

PbTe is one of the most studied thermoelectric materials for mid-temperature range applications (500-900 K) [27–29]. The band structure of PbTe is shown in Fig. 2. Both the CBM and VBM are located at the L point. Besides, they are close to each other while

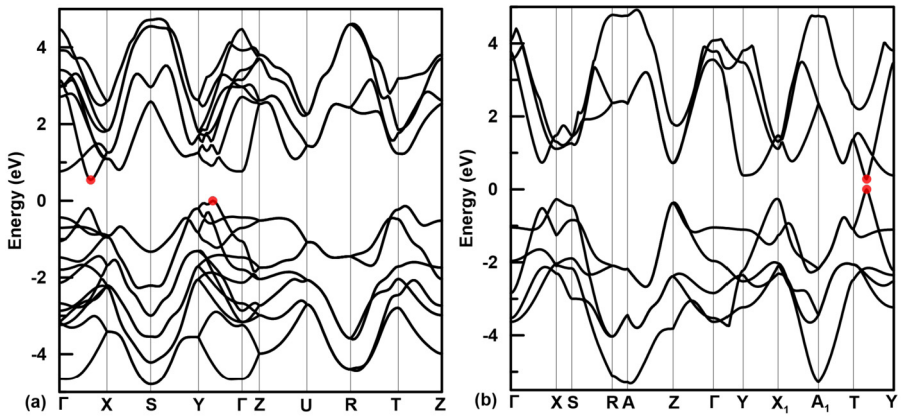


**Fig. 5.** Band structure of (a) *Pnma*-SnSe and (b) *Cmcm*-SnSe phases. The CBM and VBM are shown by red points.

**Table 2**
Key parameters of *Pnma*-SnSe and *Cmcm*-SnSe at the valence band maximum (VBM).

| | | $m^*_{\parallel}$ ($m_e$) | $m^*_{\perp}$ ($m_e$) | $m^*_c$ ($m_e$) | $m^*_d$ ($m_e$) | $\Xi$ (eV) | $N$ | $E_g$ (eV) | $c$ (GPa) | $\varepsilon_\infty$ | $\varepsilon_0$ |
|---|---|---|---|---|---|---|---|---|---|---|---|
| *Pnma* | VBM | 0.533 | 0.257 | 0.278 | 0.521 | 11.90 | 2 | 0.54 | 23.96 | 19 | 39 |
| *Cmcm* | VBM | 0.383 | 0.066 | 0.074 | 0.189 | 20.37 | 2 | 0.28 | 26.68 | 28 | 31 |

far away from the other bands. These features make PbTe an ideal material to apply the method we implemented. Moreover, there is another important feature of PbTe's band structure: it has a heavier band ($\Sigma$) along the $\Gamma$-K path, just below the VBM 0.11 eV. When the temperature rises, VBM becomes lower and aligns with the $\Sigma$ band at around 450 K, showing the so called band convergence, which has been proved by many experiments [30]. Therefore, the contribution from this $\Sigma$ band should be considered in the transport properties calculation.

Table 1 lists the key parameters required by the model for the three bands considered. The calculated values of $m^*_c$ and $m^*_d$ at the band edges are generally close to the experimental ones. The calculated values of the deformation potential constant $\Xi$ of the CBM and VBM are almost half of those from experiment, whereas $\Xi$ of the second valence band (VSB) is close to the experimental value. The calculated band gap (0.13 eV) is smaller than the experimental value (0.3 eV), most of this difference being because the calculation was done at 0 K, while the experimental value was obtained at room temperature. Fig. 3 shows the calculated relaxation time versus temperature at specified carrier concentrations: $1.8 \times 10^{19}$ cm$^{-3}$ for n-type, and $2.5 \times 10^{20}$ cm$^{-3}$ for p-type. Two sets of parameters — those from the PBE+SOC calculations and those obtained in experiment (EXPPara) — were used to calculate the relaxation times and transport properties in order to see how the difference of parameters will influence the results. As the temperature rises, the $\tau$ of the acoustic phonon scattering and polar optical phonon scattering decrease, whereas that of the impurity scattering increases for both n- and p-type. For n-type at the specified concentration, $\tau_{aco}$ and $\tau_{opt}$ are close, and $\tau_{aco}$ is lower at higher temperatures. Thus, the total relaxation time is determined by both mechanisms, with $\tau_{aco}$ contributing more at high temperatures. For p-type at the specified concentration, $\tau_{aco}$ is much smaller than $\tau_{opt}$ and $\tau_{imp}$. Therefore, the total relaxation time is determined by $\tau_{aco}$. Fig. 4 shows the calculated transport properties versus temperature at the same concentrations as in Fig. 3 for n- and p-type. The thermoelectric figure of merit $ZT = \alpha^2 \sigma T/\kappa$, and we also show the Seebeck coefficients calculated by BoltzTrap in order to compare with our model. Results of our method reflect correct trends and are close to the experimental values. In terms of Seebeck coefficient, our method gives more accurate values compared with those from BoltzTrap. Moreover, the results obtained using ab initio parameters and experimental parameters are quite similar, which indicates the robustness of the method.

### 3.2. Tin selenide (SnSe)

SnSe is a novel thermoelectric material and it has the highest reported figure of merit $ZT$ for p-type materials, about 2.6 at 923 K along the $b$ axis [31]. It has been shown in experiments that, as the temperature increases, SnSe goes through a phase transition from *Pnma* structure to *Cmcm* structure, and high $ZT$ values are observed near and above the transition temperature. Fig. 5 shows the band structures for the two phases. *Pnma* phase has an indirect band gap of 0.54 eV, whereas *Cmcm* phase has a direct band gap of 0.28 eV. From the aspect of band structure, *Cmcm* phase is more suitable for our method.

The key parameters required by the model for p-type calculations are listed in Table 2. The calculated $m^*_c$ and $m^*_d$ of *Cmcm* phase are much smaller than those of *Pnma* phase, which is beneficial for the electrical conductivity. However, the deformation potential constant $\Xi$ of *Cmcm* phase is almost twice as large as that of *Pnma* phase, which indicates a stronger acoustic phonon scattering. To compare with the experimental values, the transport properties were calculated at carrier concentrations of $3.3 \times 10^{17}$ cm$^{-3}$ for *Pnma* phase, and $5 \times 10^{18}$ cm$^{-3}$ for *Cmcm* phase, as suggested by the experimental Hall coefficient data [31]. Fig. 6 shows the relaxation time versus temperature at the specified concentrations. $\tau_{aco}$ and $\tau_{opt}$ decrease, whereas $\tau_{imp}$ increases as the temperature rises. In both *Pnma* and *Cmcm* phases, the acoustic phonon scattering dominates in the whole temperature range. Fig. 7 shows the calculated transport properties versus temperature compared with the experimental values. Experimental values belong to the $a$ and $b$ axes directions corresponding with the lowest and the highest $ZT$ directions, respectively. Also, the Seebeck coefficients calculated by BoltzTrap are listed for comparison. The calculations correctly reflect the temperature trends of the transport coefficients. For example, in experiment the Seebeck coefficient (Fig. 7a) $\alpha$ first increases with temperature, then falls because of the increasing carrier concentration and phase transition. In our model,

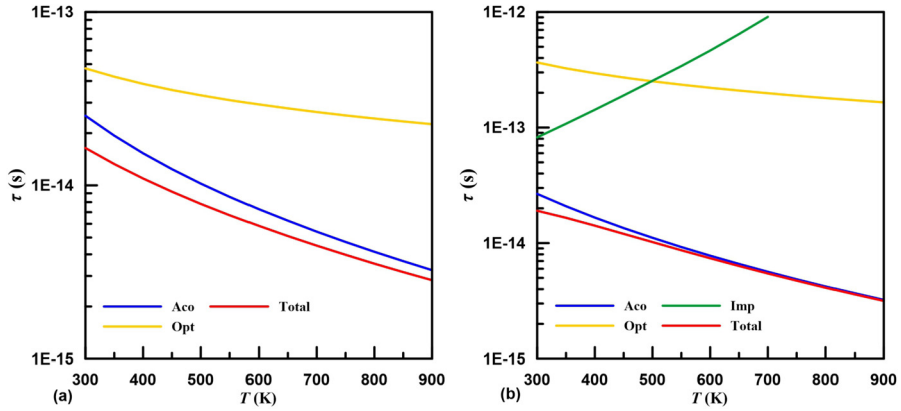


**Fig. 6.** Relaxation time for (a) *Pnma*-SnSe and (b)*Cmcm*-SnSe calculated at $= 3.3 \times 10^{17}$ cm$^{-3}$ and $p = 5 \times 10^{18}$ cm$^{-3}$, respectively.

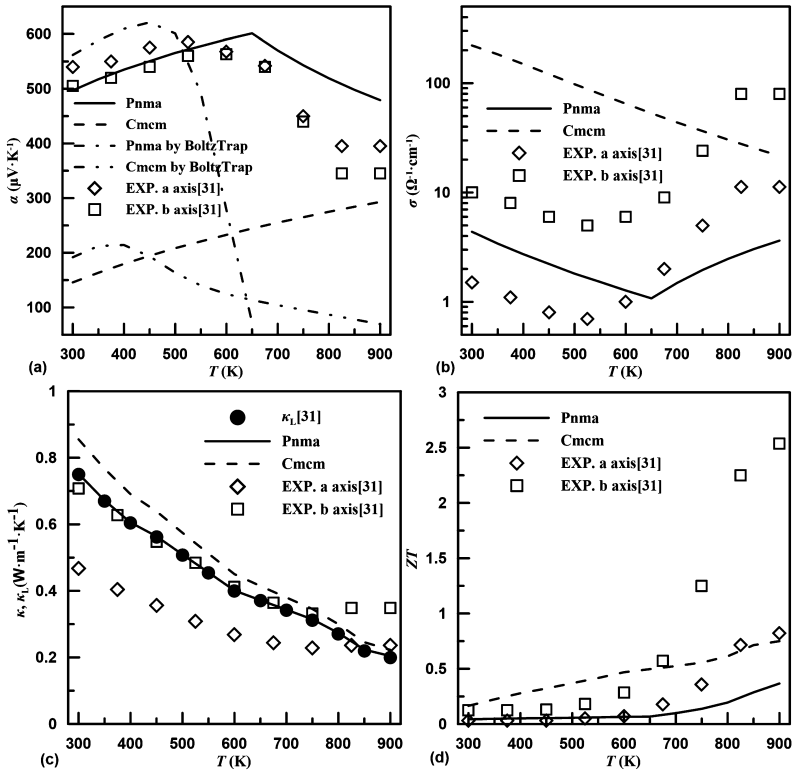


**Fig. 7.** Transport properties for *Pnma*-SnSe and *Cmcm*-SnSe calculated at $p = 3.3 \times 10^{17}$ cm$^{-3}$ and $p = 5 \times 10^{18}$ cm$^{-3}$, respectively.

the decrease of $\alpha$ of *Pnma* phase is because the carrier concentration at the middle of the gap (the starting point of chemical potential) increases as the temperature rises, and when this boundary concentration becomes higher than the specified concentration (here is $3.3 \times 10^{17}$ cm$^{-3}$), the program keeps the chemical potential at the middle of the gap and uses the boundary concentrations to calculate the properties. This leads to a cusp seen in the temperature dependencies of the electrical conductivity and Seebeck coefficient. This cusp is artificial, but reflects the intrinsic excitation of the carrier to some extent. At around 700 K, the phase transition begins and $\alpha$ becomes closer to that of *Cmcm* phase. The $\alpha$ given by our method is close to that from BoltzTrap at low temperatures, whereas the difference becomes larger at higher temperatures (after 500 K). Compared with the experimental values, BoltzTrap underestimates $\alpha$ greatly in high temperatures for both phases, while our method gives much closer values. The figure of merit *ZT* is very small at low temperatures where only *Pnma* phase exists, as both the calculation and experiment show. When the phase transition begins, the experimental *ZT* value increases greatly and the theoretical results of *Cmcm* phase become close to experiment. This example further proves the reliability of our method.

### 3.3. Bismuth telluride ($Bi_2Te_3$)

$Bi_2Te_3$ is one of the most studied and commercialized thermoelectric materials for room-temperature applications [28,32–34]. The band structure of $Bi_2Te_3$ near the Fermi surface is very complex because of the spin-orbit coupling (SOC). Therefore, it is always a challenge to calculate transport properties of $Bi_2Te_3$. The band structure is shown in Fig. 8. The calculations show that $Bi_2Te_3$ has a narrow indirect band gap of 0.16 eV. The CBM locates along the Γ-Z line (twofold degenerate), and there is a second lowest conduction band (CSB) 17

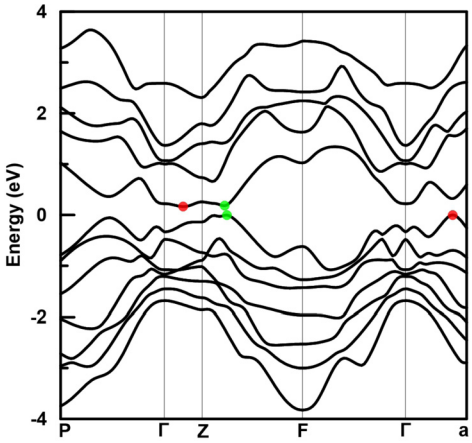


**Fig. 8.** Band structure of $Bi_2Te_3$. The CBM and VBM are shown by red points, the second highest valence band edge and second lowest conduction band edge by green points.

**Table 3**
Key parameters of $Bi_2Te_3$ at the conduction band minimum (CBM), second conduction band (CSB), valence band maximum (VBM), and second valence band (VSB).

| | $m^*_{\parallel}$ ($m_e$) | $m^*_{\perp}$ ($m_e$) | $m^*_c$ ($m_e$) | $m^*_d$ ($m_e$) | $\Xi$ (eV) | $N$ | $E_g$ (eV) | $c$ (GPa) | $\varepsilon_\infty$ | $\varepsilon_0$ |
|---|---|---|---|---|---|---|---|---|---|---|
| CBM | 0.517 | 0.351 | 0.393 | 0.634 | 13.01 | 2 | 0.165 | 27.28 | 37 | 92 |
| CSB | 4.227 | 0.047 | 0.056 | 0.695 | 10.29 | 6 | 0.182 | 27.28 | 37 | 92 |
| VBM | 0.409 | 0.061 | 0.072 | 0.378 | 13.14 | 6 | 0.165 | 27.28 | 37 | 92 |
| VSB | 1.725 | 0.047 | 0.057 | 0.512 | 12.26 | 6 | 0.168 | 27.28 | 37 | 92 |

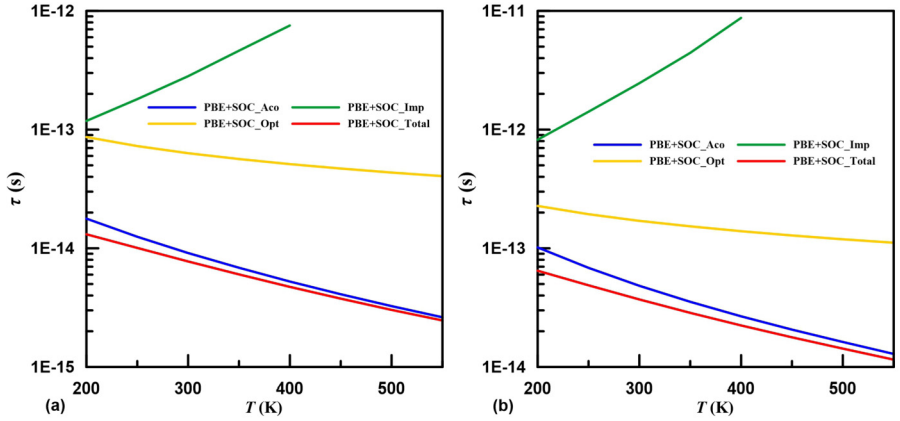


**Fig. 9.** Relaxation time for (a) n-type and (b) p-type $Bi_2Te_3$ calculated at $n = 3.3 \times 10^{19}$ cm$^{-3}$ and $p = 1.1 \times 10^{19}$ cm$^{-3}$, respectively.

meV above it along the Z-F line (sixfold degenerate). The VBM locates along the Γ-a line (sixfold degenerate), and there is also a second highest valence band (VSB) 3 meV below it along the Z-F line (sixfold degenerate). All these high-symmetry $k$-points lie in the plane containing the bisectric y axis and the trigonal z axis [34–36]. There have been conflicting reports about the exact positions of the band extrema: some studies suggest that the CBM should be along the Z-F line instead of the Γ-Z line [34,36]. These conflicts occur because of the sensitivity of the SOC which may come from different computational details, such as the method used, exchange-correlation functional, and even the lattice parameters. In the transport properties calculations, we take into account both CBM and CSB for n-type, and VBM and VSB for p-type.

The key parameters are listed in Table 3. The transport properties for p-type and n-type compounds were calculated at $1.1 \times 10^{19}$ cm$^{-3}$ and $3.3 \times 10^{19}$ cm$^{-3}$, respectively, to compare them with experimental values. Fig. 9 shows the calculated relaxation time versus temperature at specified concentration of charge carriers. The total relaxation time is dominated by acoustic phonon scattering, especially when the temperature increases. Fig. 10 shows the calculated transport properties versus temperature compared with experimental values [34,37,38]. Obvious differences between the calculated and experimental values of the transport properties become more pronounced at temperatures above 300 K. In terms of Seebeck coefficients, BoltzTrap gives better performance than our method. $Bi_2Te_3$ is a typical narrow-gap semiconductor, in which both electrons and holes are excited and the material goes into the intrinsic semiconductor regime at an elevated temperature. It has been shown in experiment that the concentrations of both electrons and holes increase greatly above 300 K [37]. This bipolar effect diminishes the Seebeck coefficient and increases the electronic thermal conductivity. In our method, the calculations for conduction and valence bands are relatively independent, therefore the bipolar effect is not included, and the trends at higher temperatures cannot be correctly reflected. However, the calculations suggest that if the bipolar effect can be suppressed, the $ZT$ values of $Bi_2Te_3$ above room temperature can be raised. This improvement can be achieved by alloying with $Sb_2Te_3$ or $Bi_2Se_3$ [33,39,40].

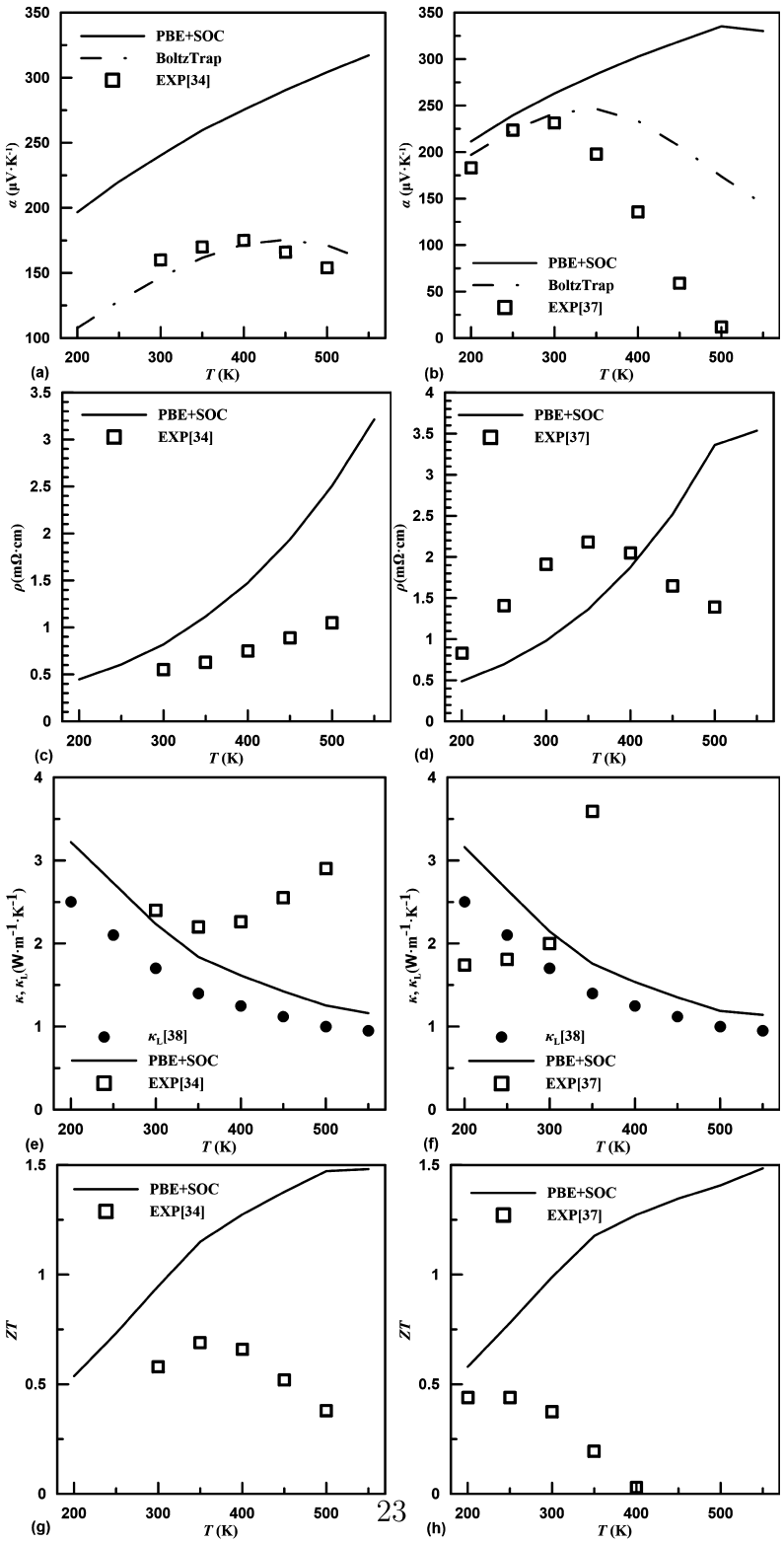


**Fig. 10.** Transport properties for n-type (left) and p-type (right) $Bi_2Te_3$ calculated at $n = 3.3 \times 10^{19}$ cm$^{-3}$ and $p = 1.1 \times 10^{19}$ cm$^{-3}$, respectively.

## 4. Conclusion

We presented an updated computer program AICON2 for calculating the transport properties of bulk materials. The previous version allows one to calculate lattice thermal conductivity in a highly efficient way. In the new version, we improved the formulas for calculating lattice thermal conductivity and added the functionality to calculate the electronic transport coefficients, such as the Seebeck coefficient and electrical conductivity, on the basis of the generalized Kane band model and perturbation theory in the framework of the relaxation time approximation. We re-optimized the original formula proposed by Ravich [7] in order to achieve highly efficient numerical calcula-

tions. In this method, we take into account three scattering mechanisms: acoustic phonon scattering, polar optical phonon scattering, and ionized impurity scattering. All key input parameters can be calculated using first-principles methods. The capabilities of the program were demonstrated on three typical thermoelectric materials and other well-known semiconductors. The reviewed cases prove the robustness and accuracy of our method.

Compared with fully ab initio software like PERTURBO, our program works much faster because we do not need to perform the computationally expensive Fermi integration in the Brillouin zone with an extremely dense mesh. In our method, the time is mainly spent on calculating such key parameters as deformation potential constant, dielectric constant, and so forth. Therefore, we also implemented a workflow management tool. All the tasks can be run automatically, with only structural files and necessary settings provided.

One of the shortcomings of the presented method is the requirement to know in advance the positions of the band extrema. This, however, is a little bit difficult for compounds with a complex band structure, especially when the band extrema are not located in the usual high symmetry paths. Moreover, the current method, while showing reliable results for semiconductors, does not work for metals. We are working on combining the deformation potential theory with fully ab initio transport calculations and hope to overcome the mentioned issues in the next major release.

Overall, the program will be useful for a high-throughput screening of thermoelectric materials.

## Declaration of competing interest

The authors declare that they have no known competing financial interests or personal relationships that could have appeared to influence the work reported in this paper.

## Acknowledgements

We acknowledge the usage of the Skoltech HPC cluster ARKUDA for obtaining the results presented in this paper. This work is funded by Russian Science Foundation (grant 19-72-30043) and the Ministry of Science and Education to leading scientific schools (grant 2711.2020.2).

## Appendix A. Supplementary material

Supplementary material related to this article can be found online at https://doi.org/10.1016/j.cpc.2021.108027.

## References

[1] T. Fan, A.R. Oganov, Comput. Phys. Commun. 251 (2020) 107074.
[2] G.K. Madsen, J. Carrete, M.J. Verstraete, Comput. Phys. Commun. 231 (2018) 140–145.
[3] G. Pizzi, D. Volja, B. Kozinsky, M. Fornari, N. Marzari, Comput. Phys. Commun. 185 (1) (2014) 422–429.
[4] J.-J. Zhou, J. Park, I.-T. Lu, I. Maliyov, X. Tong, M. Bernardi, Perturbo: a software package for ab initio electron-phonon interactions, charge transport and ultrafast dynamics, arXiv preprint, arXiv:2002.02045, 2020.
[5] J. Bardeen, W. Shockley, Phys. Rev. 80 (1) (1950) 72.
[6] C. Herring, E. Vogt, Phys. Rev. 101 (3) (1956) 944.
[7] Y.I. Ravich, B. Efimova, V. Tamarchenko, Phys. Status Solidi (b) 43 (1) (1971) 11–33.
[8] I.I. Ravich, Semiconducting Lead Chalcogenides, vol. 5, Springer Science & Business Media, 2013.
[9] D. Bilc, S. Mahanti, M. Kanatzidis, Phys. Rev. B 74 (12) (2006) 125202.
[10] Y. Pei, X. Shi, A. LaLonde, H. Wang, L. Chen, G.J. Snyder, Nature 473 (7345) (2011) 66–69.
[11] Y. Pei, A.D. LaLonde, H. Wang, G.J. Snyder, Energy Environ. Sci. 5 (7) (2012) 7963–7969.
[12] W. He, D. Wang, H. Wu, Y. Xiao, Y. Zhang, D. He, Y. Feng, Y.-J. Hao, J.-F. Dong, R. Chetty, et al., Science 365 (6460) (2019) 1418–1424.
[13] I.T. Witting, F. Ricci, T.C. Chasapis, G. Hautier, G.J. Snyder, et al., Research 2020 (2020) 4361703.
[14] K. Mathew, J.H. Montoya, A. Faghaninia, S. Dwarakanath, M. Aykol, H. Tang, I.-h. Chu, T. Smidt, B. Bocklund, M. Horton, et al., Comput. Mater. Sci. 139 (2017) 140–152.
[15] A. Jain, S.P. Ong, W. Chen, B. Medasani, X. Qu, M. Kocher, M. Brafman, G. Petretto, G.-M. Rignanese, G. Hautier, et al., Concurr. Comput., Pract. Exp. 27 (17) (2015) 5037–5059.
[16] W. Voigt, Lehrbuch der Kristallphysik: (Mit Ausschluss der Kristalloptik), vol. 34, BG Teubner, 1910.
[17] A. Reuss, Z. Angew. Math. Mech. 9 (1929) 49–58.
[18] R. Hill, Proc. Phys. Soc. A 65 (5) (1952) 349.
[19] A. Fonari, C. Sutton, Effective mass calculator, can be found under, https://github.com/afonari/, 2012.
[20] W. McKinney, et al., Python High. Perform. Sci. Comput. 14 (9) (2011).
[21] S.P. Ong, W.D. Richards, A. Jain, G. Hautier, M. Kocher, S. Cholia, D. Gunter, V.L. Chevrier, K.A. Persson, G. Ceder, Comput. Mater. Sci. 68 (2013) 314–319.
[22] G. Kresse, J. Furthmüller, Phys. Rev. B 54 (16) (1996) 11169.
[23] G. Kresse, J. Furthmüller, Comput. Mater. Sci. 6 (1) (1996) 15–50.
[24] J.P. Perdew, K. Burke, M. Ernzerhof, Phys. Rev. Lett. 77 (18) (1996) 3865.
[25] X. Gonze, C. Lee, Phys. Rev. B 55 (16) (1997) 10355.
[26] S. Grimme, J. Antony, S. Ehrlich, H. Krieg, J. Chem. Phys. 132 (15) (2010) 154104.
[27] G. Nimtz, B. Schlicht, in: Narrow-Gap Semiconductors, Springer, 1983, pp. 1–117.
[28] G.J. Snyder, E.S. Toberer, in: Materials for Sustainable Energy: a Collection of Peer-Reviewed Research and Review Articles from Nature Publishing Group, World Scientific, 2011, pp. 101–110.
[29] G. Tan, L.-D. Zhao, M.G. Kanatzidis, Chem. Rev. 116 (19) (2016) 12123–12149.
[30] Y. Pei, H. Wang, G.J. Snyder, Adv. Mater. 24 (46) (2012) 6125–6135.
[31] L.-D. Zhao, S.-H. Lo, Y. Zhang, H. Sun, G. Tan, C. Uher, C. Wolverton, V.P. Dravid, M.G. Kanatzidis, Nature 508 (7496) (2014) 373.
[32] T. Zhu, L. Hu, X. Zhao, J. He, Adv. Sci. 3 (7) (2016) 1600004.
[33] C. Han, Q. Sun, Z. Li, S.X. Dou, Adv. Energy Mater. 6 (15) (2016) 1600498.
[34] I.T. Witting, T.C. Chasapis, F. Ricci, M. Peters, N.A. Heinz, G. Hautier, G.J. Snyder, Adv. Electron. Mater. 5 (6) (2019) 1800904.
[35] M. Michiardi, I. Aguilera, M. Bianchi, V.E. de Carvalho, L.O. Ladeira, N.G. Teixeira, E.A. Soares, C. Friedrich, S. Blügel, P. Hofmann, Phys. Rev. B 90 (7) (2014) 075105.
[36] G. Wang, T. Cagin, Phys. Rev. B 76 (7) (2007) 075201.
[37] H.-W. Jeon, H.-P. Ha, D.-B. Hyun, J.-D. Shim, J. Phys. Chem. Solids 52 (4) (1991) 579–585.
[38] B.-L. Huang, M. Kaviany, Phys. Rev. B 77 (12) (2008) 125209.
[39] O. Yamashita, S. Tomiyoshi, J. Appl. Phys. 95 (1) (2004) 161–169.
[40] X. Shi, L. Chen, C. Uher, Int. Mater. Rev. 61 (6) (2016) 379–415.